New Journal of Physics
The open access journal at the forefront of physics
Deutsche Physikalische Gesellschaft DPG | IOP Institute of Physics

Electrically tunable conductance and edge modes in topological crystalline insulator thin films: minimal tight-binding model analysis

Motohiko Ezawa
Department of Applied Physics, University of Tokyo, Hongo 7-3-1, 113-8656, Japan
E-mail: ezawa@ap.t.u-tokyo.ac.jp

Received 15 March 2014, revised 26 April 2014
Accepted for publication 30 April 2014
Published 24 June 2014
New Journal of Physics **16** (2014) 065015
doi:10.1088/1367-2630/16/6/065015

Abstract
Topological crystalline insulators (TCI) have been experimentally manufactured and studied. We propose a minimal tight-binding model for thin films made of TCI on the basis of the mirror and discrete rotational symmetries. The basic term consists of the spin–orbit interaction describing a Weyl semimetal, where gapless Dirac cones emerge at all the high-symmetry points in the momentum space. We then introduce the mass term providing gaps to Dirac cones. They simulate the thin films made of the [001], [111] and [110] TCI surfaces. TCI thin films are two-dimensional topological insulators protected by mirror symmetry. The mirror symmetry is broken by introducing an electric field E_z perpendicular to the film. We first note that the band structure can be controlled using the electric field. We then analyze the mirror-Chern number and the edge modes taking into consideration the bulk–edge correspondence, even for $E_z \neq 0$. We also calculate the conductance as a function of E_z. We propose a multi-digit topological field-effect transistor by applying an electric field independently to the right and left edges of a nanoribbon. Our results will open up a new route to topological electronics.

Keywords: topological crystalline insulator, mirror-Chern number, topological insulator

1. Introduction

The topological insulator is one of the most fascinating concepts found in this decade [1, 2]. The recent flourishing of research on it is based on the discovery of the time-reversal invariant topological insulator [3–6]. Electrons obey the Dirac equation in almost all topological insulators. A system may contain several Dirac cones in the momentum space. In such a case we may assign a topological number to each of them. Let N be the number of Dirac cones. The total topological number is the Chern number, and there appear $N-1$ valley-Chern numbers. (There are also spin-Chern and spin–valley-Chern numbers if the spin is a good quantum number.) The valley degree of freedom leads to valleytronics [7–20]. The decisive advantage of a topological object is that its stability is protected topologically against dissipation and fluctuation even in the presence of large defects as long as the relevant symmetries are unbroken [21–26]. Hence they may serve as key components in designing nanodevices for future topological electronics. Since electronics is based on circuits in two dimensions, two-dimensional (2D) topological insulators will be particularly important. The best candidate is silicene containing two Dirac cones. An electrically tunable band gap and a topological phase transition are proposed [27, 28]. Edge states show various characters depending on the topological phase [29, 30]. This provides an ideal playground in which to develop various ideas on topological electronics and valleytronics [14, 31]. In spite of all the merits, however, silicene has so far been manufactured only on a metallic substrate, such as silver [32, 33], whose effect seems to obscure the topological character [34].

Very recently, a new class of topological insulators, namely the topological crystalline insulators (TCI), has been discovered [35–50]. An example is provided by $Pb_xSn_{1-x}Te$. There are three kinds of surface states, namely the [001], [111] and [110] surfaces, which have discrete rotation symmetries C_N with $N = 4$, 6 and 2, respectively. Gapless Dirac cones emerge inevitably on the surface of a topological insulator. Indeed, it has been experimentally observed that there are gapless Dirac cones at the X and Y points in the [001] surface [37–39], and at the Γ and three M points in the [111] surface [40, 41].

Although there are as yet no experimental measurements, theoretical studies [42, 43] have been presented on thin film made of TCI. It is characterized by the same discrete rotation symmetry C_N, and additionally by the mirror symmetry about the 2D plane. When the film is thin enough, the gap opens due to hybridization between the front and back surfaces, and this turns the system into a 2D topological insulator protected by the mirror symmetry. Accordingly the topological number is the mirror-Chern number [51, 52]. A prominent feature is that we can break the mirror symmetry simply by applying an external electric field. This is greatly in contrast to the case of the time-reversal invariant topological insulator, where the time-reversal breaking should be caused by the magnetic field or the exchange field induced by a ferromagnet. The magnetic field and the exchange field are hard to control precisely. On the other hand, a precise control of the electric field is possible within current techniques.

The aim of this work is to explore the physics of the TCI thin film by applying various ideas cultivated in the study of silicene. For this purpose we start with constructing a minimal tight-binding model based on the discrete rotation symmetry C_N and the mirror symmetry about the 2D plane. The tight-binding model is essential for obtaining a deeper understanding of the system, which is not attained by first-principles calculation and low-energy effective Dirac theory. For instance, according to the low-energy theory [42], the [001] thin film made of

$Pb_xSn_{1-x}Te$ has two Dirac cones at the X and Y points, where the chiralities are identical. However, the Nielsen–Ninomiya theorem [53] dictates that the total chirality is zero. Consequently, there must be two additional Dirac cones with chirality opposite to that of the X and Y points. In our tight-binding model these two Dirac cones emerge at the Γ and M points, though they are removed from the low-energy spectrum. Furthermore, all of these Dirac cones contribute to the Chern number, which is obtained by integrating the Berry curvature over all occupied states of electrons in the momentum space. The tight-binding model is also useful for analyzing the edge states, which transport the ordinary electric current reflecting the topological properties of the thin film.

This paper is composed as follows. In section 2, we propose 2D Hamiltonian systems where the spin–orbit interaction (SOI) dominates the transfer term. We demonstrate that such a system is a Weyl semimetal consisting of multiple Dirac cones at all the high-symmetry points. In section 3, we analyze the square lattice with the C_4 symmetry. Four Dirac cones appear at the X, Y, Γ and M points. We introduce mass terms to give gaps to the Dirac cones. The system may describe well the TCI thin film made of $Pb_xSn_{1-x}Te$ with an appropriate choice of phenomenological mass parameters. We investigate the topological numbers. They are the mirror-Chern number and three valley–mirror-Chern numbers. (We note that the spin is not a good quantum number.) All of these are symmetry-protected topological numbers [26]. They are no longer quantized but change continuously when we break the mirror symmetry by introducing the perpendicular electric field E_z. We also investigate the gap structure of nanoribbons in order to explore how gapless edge modes emerge and transport electric charges. The conductance is calculated in the presence of E_z. The conductance is switched off by the electric field. Namely, it acts as a topological field-effect transistor [54]. By attaching two independent gates to the sample, we can separately control the right and left edge states. The conductance can be 0, 1 and 2, which forms a multi-digit topological field-effect transistor, where the conductance is quantized and topologically protected. In section 4, we analyze the triangular lattice with the C_6 symmetry. The system contains six Dirac cones at the Γ, K, K′, M_1, M_2, M_3 points. We thus have the mirror-Chern number and five valley–mirror-Chern numbers. All other studies are quite similar to those of the square lattice with the C_4 symmetry. In section 5, we briefly discuss the square lattice with the C_2 symmetry.

2. Tight-binding hamiltonians

Our main proposal is a phenomenological construction of minimal tight-binding Hamiltonians for the TCI thin film, based upon which we carry out an analysis of electrically controllable conductance and edge modes of a nanoribbon considering the bulk–edge correspondence. In this section we construct the tight-binding Hamiltonian such that it is invariant under the discrete rotation symmetry C_N in addition to the mirror symmetry M to be defined later in (11). The generator of C_N is

$$C_N = R_z \exp\left[-\frac{\mathrm{i}\pi}{N}\sigma_z \right], \tag{1}$$

with the $\frac{2\pi}{N}$-rotation of the momentum:

$$R_z: \begin{pmatrix} k_x \\ k_y \end{pmatrix} \mapsto \begin{pmatrix} \cos\dfrac{2\pi}{N} & \sin\dfrac{2\pi}{N} \\ -\sin\dfrac{2\pi}{N} & \cos\dfrac{2\pi}{N} \end{pmatrix} \begin{pmatrix} k_x \\ k_y \end{pmatrix}. \tag{2}$$

We note that the C_N transformation rotates the direction of spin by π/N. The rotation angle is restricted to being $N = 2, 3, 4, 6$ due to the crystal group of the lattice symmetry, corresponding to the rectangular lattice for $N = 2$, the hexagonal lattice for $N = 3$, the square lattice for $N = 4$, and the triangular lattice for $N = 6$.

The SOI plays a key role in the physics of topological insulators. We consider a model where the SOI dominates the system. The simplest example is the Rashba SOI:

$$H_{\rm SO} = {\rm i}\sum_{\ell=1}\lambda_\ell \sum_{\langle i,j\rangle} c_i^\dagger \left[\sigma \times \boldsymbol{d}_{ij}^\ell\right] c_j. \tag{3}$$

Alternatively we may think of

$$H_{\rm SO} = {\rm i}\sum_{\ell=1}\lambda_\ell \sum_{\langle i,j\rangle} c_i^\dagger \left[\sigma \cdot \boldsymbol{d}_{ij}^\ell\right] c_j, \tag{4}$$

or even take a sum of these. Here, $\sigma = \left(\sigma_x, \sigma_y, \sigma_z\right)$ represents the Pauli matrix for the spin, and $\boldsymbol{d}_{ij}^\ell = \boldsymbol{r}_i - \boldsymbol{r}_j$ connects a pair of the ℓ th-nearest neighbor sites i and j in the lattice with λ_ℓ the coupling strength. As is easily shown (see section 5), the results based on the Hamiltonian (3) are obtained from those on the Hamiltonian (4) simply with the replacement of a set of momenta $\left(k_x, k_y\right)$ by $\left(k_y, -k_x\right)$. Furthermore, the low-energy theory derived from a first-principles calculation [42] supports the choice of (4) rather than (3). Hence we concentrate on (4) hereafter.

Let N_ℓ be the number of ℓ th neighbor sites. In the momentum representation the Hamiltonian is rewritten as

$$H_{\rm SO} = \sum_{\boldsymbol{k}} c^\dagger(\boldsymbol{k})\hat{H}_{\rm SO}(\boldsymbol{k})c(\boldsymbol{k}), \tag{5}$$

with

$$\hat{H}_{\rm SO}(\boldsymbol{k}) = \sum_{\ell=1}\lambda_\ell \sum_{n=1}^{N_\ell} \sigma \cdot \boldsymbol{d}_n^\ell e^{i\boldsymbol{d}_n^\ell \cdot \boldsymbol{k}}, \tag{6}$$

where $\boldsymbol{d}_{ij}^\ell$ is determined by requiring invariance under the discrete rotational symmetry C_N. For instance, $\boldsymbol{d}_n^\ell$ for the nearest neighbor sites ($\ell = 1$) is expressed as

$$\boldsymbol{d}_n^1 = \left|\boldsymbol{d}_n^1\right|\left(\cos\theta_n, \sin\theta_n\right), \quad \theta_n = \frac{2\pi n}{N} \tag{7}$$

for the triangular ($N = 3$) and square ($N = 4$) lattices: see figures 1(a) and (c). We shall soon see that this model has multiple Dirac cones at the high-symmetry points known, such as the X, Y, Γ and M points in the square lattice and the Γ, K, K′, M_1, M_2, M_3 points in the triangular lattice [55]. The Hamiltonian (3) describes a Weyl semimetal.

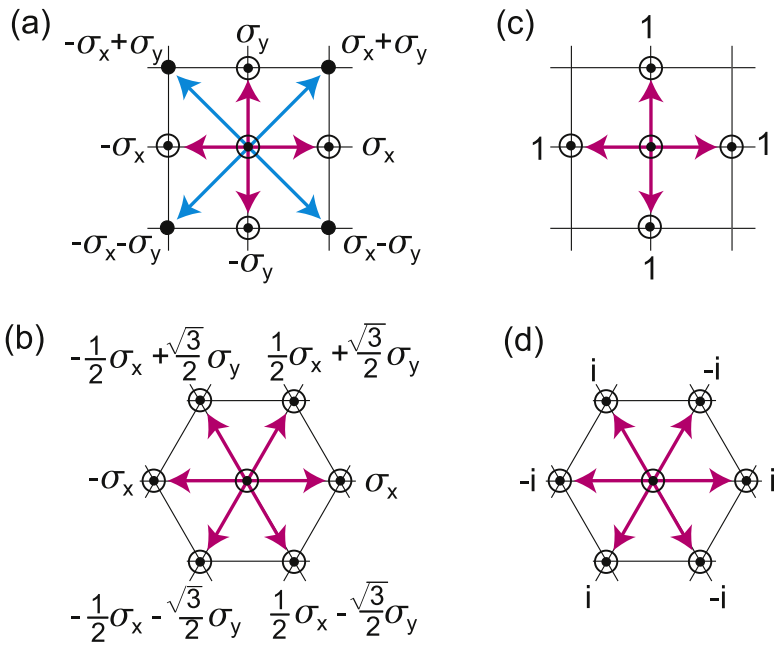

Figure 1. Nearest and next-nearest neighbor sites in real space. We give the value of $\sigma \cdot \boldsymbol{d}_{ij}^{\ell}$ for the nearest ($\ell = 1$, magenta) and next-nearest ($\ell = 2$, cyan) neighbor sites for the square lattice (a) and the triangular lattice (b) in the Hamiltonian (4). We also give the value of ν_{ij} for the nearest neighbor site ($\ell = 1$, magenta) for the square lattice (c) and the triangular lattice (d) in the Hamiltonian (9).

The minimal tight-binding Hamiltonian of a TCI thin film would be a four-band model due to the spin and pseudospin (surface) degrees of freedom. Let $\tau = \left(\tau_x, \tau_y, \tau_z\right)$ be the Pauli matrix for describing the pseudospin representing the front ($\tau_z = 1$) and back ($\tau_z = -1$) surfaces. When the film is thin enough, the symmetric state becomes the ground state, opening a gap in all Dirac cones due to hybridization. We employ the Hamiltonian (3) to describe the symmetric state. Furthermore we apply the electric field E_z between the two surfaces.

These effects are realized by considering the four-band effective tight-binding Hamiltonian,

$$\hat{H} = \hat{H}_{\rm SO}\tau_y + \hat{H}_m\tau_x + E_z\tau_z, \tag{8}$$

together with $\hat{H}_{\rm SO}$ given by (6) and $\hat{H}_m$ obtained from

$$H_m = \sum_{\ell=0} m_\ell \sum_{\langle i,j\rangle} \nu_{ij}^{\ell} c_i^{\dagger} c_j, \tag{9}$$

where ν_{ij}^{ℓ} is a number characteristic for the lattice structure and determined by the vector $\boldsymbol{d}_{ij}^{\ell}$, so as to preserve the crystalline symmetry, and i, j runs over the sites of the ℓth-nearest neighbors. We take $\nu_{ij}^{0} = \delta_{ij}$ and show ν_{ij}^{1} in figures 1(c) and (d) for the square and triangular lattices. As we shall soon see, the gap at each Dirac point is adjusted by choosing the mass parameters m_ℓ appropriately.

In the absence of the external electric field ($E_z = 0$), the Hamiltonian (8) is invariant under the mirror symmetry about the 2D plane:

$$MH\left(\boldsymbol{k}\right)M^{-1} = H\left(\boldsymbol{k}\right), \tag{10}$$

where the mirror operator is given by

$$M = -\frac{\mathrm{i}}{2}\sigma_z\tau_x. \tag{11}$$

The mirror symmetry is broken by the external electric field ($E_z \neq 0$) as follows:

$$M\left(E_z\tau_z\right)M^{-1} = -E_z\tau_z. \tag{12}$$

When the system is an insulator, the mirror-Chern charge is defined and calculable even in a broken phase of the mirror symmetry [26].

3. The square lattice with C_4 symmetry

We first consider the square lattice with the C_4 symmetry. Let us set $E_z = 0$. First, taking the contributions from the nearest neighbor sites ($\ell = 1$) and the next-nearest neighbor sites ($\ell = 2$), we obtain from the Hamiltonian (4)

$$\hat{H}_{\mathrm{SO}} = A_x\sigma_x + A_y\sigma_y \tag{13}$$

with

$$A_x = \lambda_1 \sin k_x + \lambda_2 \sin k_x \cos k_y, \tag{14}$$

$$A_y = \lambda_1 \sin k_y + \lambda_2 \sin k_y \cos k_x. \tag{15}$$

See the illustration in figures 1(a) and (b). The energy spectrum is given by

$$E = \pm\sqrt{A_x^2 + A_y^2}\,. \tag{16}$$

There are gapless Dirac cones at the X, Y, Γ and M points, as illustrated in figure 2, where the band structure is shown. The Hamiltonian describes a Weyl semimetal.

The effective low-energy Hamiltonian is given by (13) near each Dirac point with

$$A_x = v_x\tilde{k}_x, \quad A_y = v_y\tilde{k}_y, \tag{17}$$

where v_x and v_y are the velocities

$$v_x = n_x\left(\lambda_1 + n_y\lambda_2\right), \quad v_y = n_y\left(\lambda_1 + n_x\lambda_2\right), \tag{18}$$

and $\tilde{k}_x$ and $\tilde{k}_y$ are the renormalized momenta

$$\tilde{k}_x = k_x + \frac{n_x - 1}{2}\pi, \quad \tilde{k}_y = k_y + \frac{n_y - 1}{2}\pi, \tag{19}$$

as follows from (14). One set of numbers $\left(n_x, n_y\right)$ is $\left(-1, 1\right)$ for X, $\left(1, -1\right)$ for Y, $\left(1, 1\right)$ for Γ, $\left(-1, -1\right)$ for M. The chirality of the Dirac cone is given by n_xn_y at each point. An anisotropy ($v_x \neq v_y$) has been introduced into the system by introducing the nearest and next-nearest neighbor contributions ($\lambda_1 \neq 0$, $\lambda_2 \neq 0$).

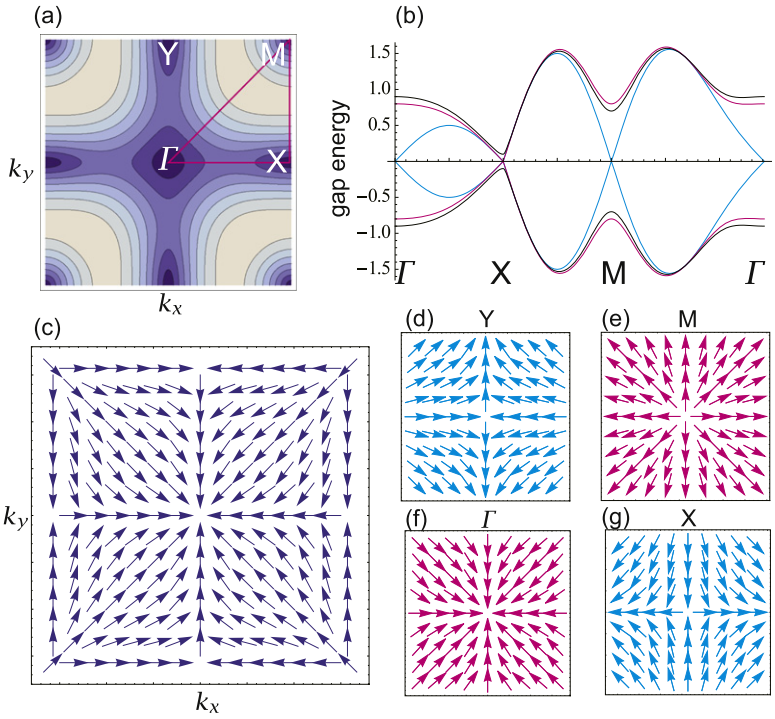

Figure 2. Band structure and spin direction on a square lattice. (a) A contour plot of the band structure of the Hamiltonian (8) on the square lattice. We have set $\lambda_1 = \lambda_2 = 0$, $m_1 = m_2 = 0$. The energy is lower in darker regions. (b) The band structure along the lines shown in magenta in (a). We have set $\lambda_1 = \lambda_2 = 0$ for all three curves. Cyan curves are for $m_1 = m_2 = 0$. Magenta curves are for $m_1 = 0.4$, $m_0 = 0$. Black curves are for $m_1 = 0.4$, $m_0 = 0.1$. (c) The spin direction in the thin film with the C_4 symmetry for the whole Brillouin zone, around (d) the Y point, (e) the M point, (f) the Γ point and (g) the X point. The spin structure is hedgehog-like around the Γ and M points with the opposite directions, both yielding positive chirality (magenta), while it is anti-hedgehog-like around the X and Y points with the opposite directions, both yielding negative chirality (cyan). They contribute to the mirror-Chern number.

We illustrate the spin direction around each Dirac point in figure 2. The spin direction yields one negative chirality apiece at the X and Y points, while it yields one positive chirality apiece at the Γ and M points. The total chirality is zero over the Brillouin zone, as required by the Nielsen–Ninomiya theorem [53].

We proceed to consider the total Hamiltonian (8) with $E_z = 0$, which reads

$$\hat{H} = \left[A_x\sigma_x + A_y\sigma_y\right]\tau_y + m\tau_x, \tag{20}$$

with (14) and

$$m = m_0 + m_1\left(\cos k_x + \cos k_y\right). \tag{21}$$

The energy spectrum is now given by

$$E = \pm\sqrt{A_x^2 + A_y^2 + m^2}\,. \tag{22}$$

We see that m_1 opens a gap at the Γ and M points, while m_0 opens a gap at all Dirac points, as illustrated in figure 2(b). Note that, if we set $m_0 = 0$, massless Dirac cones appear at the X and Y points (figure 2(b)). The term $m_0\tau_x$ is understood to simulate the effect of a gap opening due to hybridization between the front and back surfaces in a thin film. The Dirac cones at the Γ and M points are removed from the low-energy theory when we take a large value of m_1.

The low-energy Dirac theory is extracted from (20) around the X and Y points as

$$H_X = \left(v_1 k_x \sigma_x - v_2 k_y \sigma_y\right)\tau_y + m\tau_x, \tag{23}$$

$$H_Y = \left(v_2 k_x \sigma_x - v_1 k_y \sigma_y\right)\tau_y + m\tau_x, \tag{24}$$

with the velocities v_1 and v_2 being given by

$$v_1 = \lambda_1 - \lambda_2, \quad v_2 = \lambda_1 + \lambda_2. \tag{25}$$

It is worth noting that this low-energy Hamiltonian agrees with the one derived on the basis of a first-principles calculation and the Dirac theory of the TCI surface [42].

Our Hamiltonian is capable of simulating various models by controlling m_ℓ. For instance, a massless Dirac cone emerges only at the Γ point on setting $m_0 = -2m_1$, as illustrated in figures 3(a3) and (b3). Similarly a massless Dirac cone emerges only at the M point on setting $m_0 = 2m_1$, as illustrated in figures 3(a4) and (b4).

Next we introduce an external electric field E_z perpendicular to the film. The energy spectrum is given by

$$E = \pm\sqrt{A_x^2 + A_y^2 + m^2 + E_z^2}, \tag{26}$$

which shows that the band gap is controllable by applying an external field.

3.1. Mirror-Chern numbers

The thin film is an insulator, since a gap is given to all Dirac points by the term $m_0\tau_x$. When $E_z = 0$, the mirror symmetry is a good symmetry. Namely, the mirror operator (11) commutes with the Hamiltonian, $[H, M] = 0$, which enables us to divide the Hilbert space by the eigenvalues ($M = \pm$ i) of the mirror operator [52]. The mirror-Chern number C_M is defined by the difference of the Chern numbers in these two sectors,

$$C_M = \frac{1}{2}\left(C_{\mathrm{i}} - C_{-\mathrm{i}}\right), \tag{27}$$

where $C_{\pm}$i is the Chern number for the subspace with the mirror eigenvalue $M = \pm$ i.

The mirror-Chern charge can actually be defined even for $E_z \neq 0$. It is given by [26]

$$C_M = \frac{1}{6(2\pi)^2}\varepsilon_{\mu\nu\rho}\int \mathrm{d}^2k \int_{-\infty}^{\infty} \mathrm{d}\omega \ \ \mathrm{Tr}\left[G\Gamma_\mu G\Gamma_\nu G\Gamma_\rho\right] \tag{28}$$

in terms of the Matsubara Green function,

$$G\left(\boldsymbol{k}\right) = \frac{1}{\mathrm{i}\omega - H\left(\boldsymbol{k}\right)}, \tag{29}$$

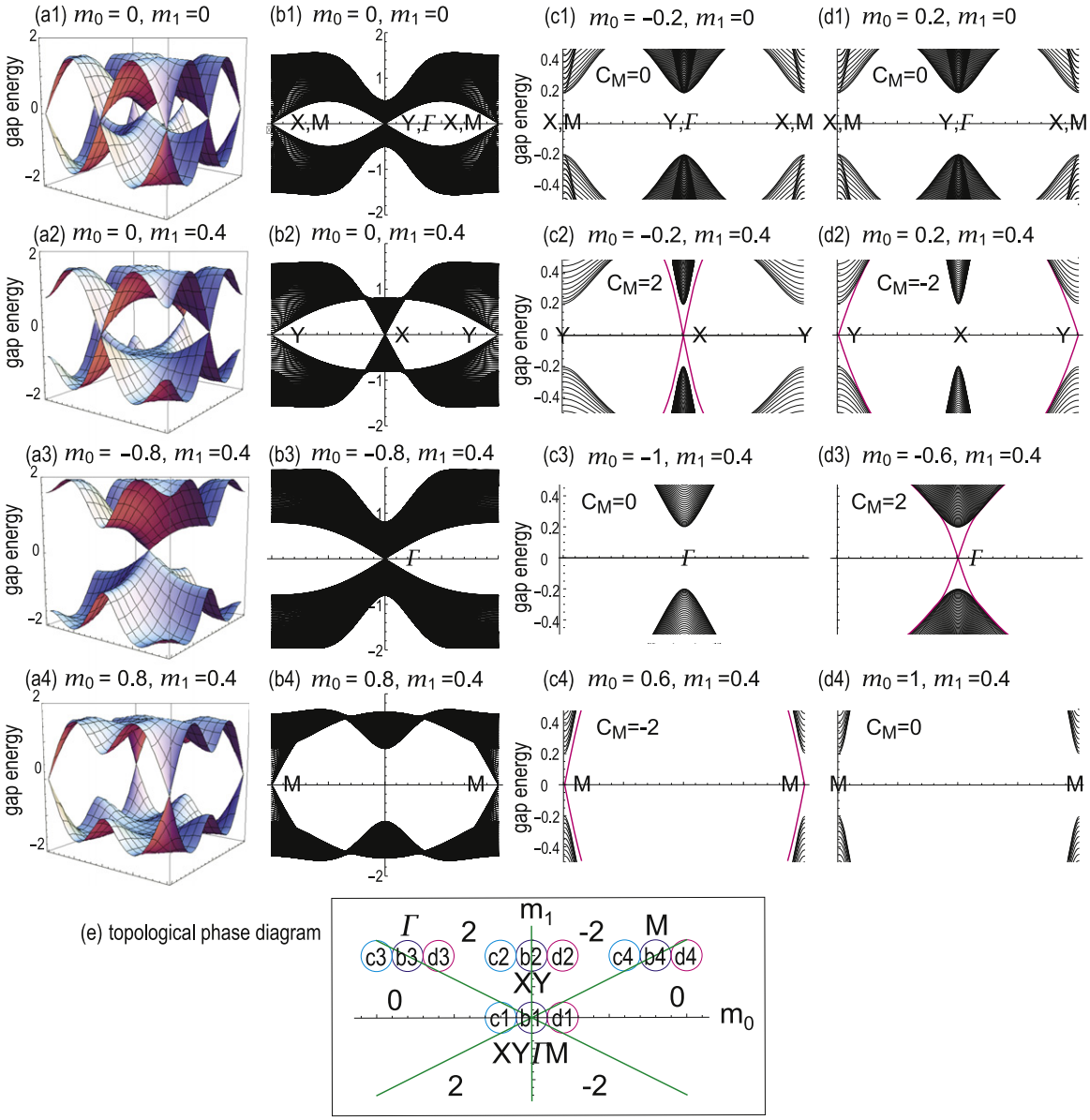

Figure 3. Band structure and topological phase diagram for the square lattice. (a) Bird's eye views and (b) projected views of the bulk band structure. ((c), (d)) The band structure of nanoribbons, where the gapless edge states are depicted using magenta curves. They emerge in topological insulators with nonzero mirror-Chern numbers. We have taken $\lambda_1 = 1$ and $\lambda_2 = -0.5$ in all figures. The values of m_0 and m_1 are indicated in each figure. The vertical axis is the energy in units of λ_1 in all figures. The horizontal axes are $-\pi < k_x \leqslant \pi$, $-\pi < k_y \leqslant \pi$ in (a), $-\pi < k_x \leqslant \pi$ in (b), $-\pi < k \leqslant \pi$ in (c) and (d). (e) The topological phase diagram in the m_0–m_1 plane. A green line represents a phase boundary. The numbers 0 and ± 2 are the mirror-Chern numbers. A circle with a symbol, such as c3, shows a point where the band structure is calculated in (c3).

where iω refers to the Matsubara frequency (ω: real), H is the Hamiltonian, and

$$\Gamma_x = \frac{1}{2}\left\{M, \partial_x G^{-1}\right\}, \quad \Gamma_y = \partial_y G^{-1}, \quad \Gamma_0 = \partial_0 G^{-1}, \tag{30}$$

with M the mirror-symmetry generator (11). When the mirror symmetry is a good symmetry, the formula (28) agrees with the standard definition (27).

To analyze the low-energy physics near the Fermi level, we may take the Dirac Hamiltonian at each Dirac point as the Hamiltonian H in (29). Then we obtain four mirror-Chern numbers, which are explicitly calculated [26] as

$$C_M\left(n_x, n_y; E_z\right) = \frac{1}{2} n_x n_y \frac{m}{\sqrt{m^2 + E_z^2}} \tag{31}$$

for Dirac cones characterized by $n_x = \pm 1$ and $n_y = \pm 1$ with m given by (21). As $E_z \to 0$, they are reduced to $C_M\left(n_x, n_y\right) = n_x n_y \ \mathrm{sgn}\left(m\right)$ and quantized. They explicitly read as

$$C_M\left(1, 1\right) = \frac{1}{2} \ \mathrm{sgn}\left(m_0 - 2m_1\right), \qquad C_M\left(-1, -1\right) = \frac{1}{2} \ \mathrm{sgn}\left(m_0 + 2m_1\right), \tag{32}$$

$$C_M\left(1, -1\right) = C_M\left(-1, 1\right) = -\frac{1}{2} \ \mathrm{sgn}\left(m_0\right), \tag{33}$$

each of which is a symmetry-protected topological charge.

When we adopt the tight-binding Hamiltonian as H in (29), the mirror-Chern number is the sum of these four terms:

$$C_M = \sum_{n_x=\pm 1, n_y=\pm 1} C_M\left(n_x, n_y\right) = \frac{1}{2} \ \mathrm{sgn}\left(m_0 + 2m_1\right) + \frac{1}{2} \ \mathrm{sgn}\left(m_0 - 2m_1\right) - \mathrm{sgn}\left(m_0\right). \tag{34}$$

We show the topological phase diagram in the $\left(m_0, m_1\right)$ plane with respect to C_M in figure 3(e). The edge states protected by the mirror symmetry emerge when the mirror-Chern number is nonzero. The sign of the mirror-Chern number reflects the place where the edge modes emerge: the edge modes emerge at the Y point when $C_M > 0$, while the edge modes emerge at the X point when $C_M < 0$.

At low energy near the Fermi level, since the four Dirac Hamiltonians describe the system, we can additionally define three valley–mirror-Chern numbers:

$$C_{VM1} = \sum_{n_x=\pm 1, n_y=\pm 1} n_x C_M\left(n_x, n_y\right) = -\frac{1}{2} \ \mathrm{sgn}\left(m_0 + 2m_1\right) + \frac{1}{2} \ \mathrm{sgn}\left(m_0 - 2m_1\right), \tag{35}$$

$$C_{VM2} = \sum_{n_x=\pm 1, n_y=\pm 1} n_y C_M\left(n_x, n_y\right) = -\frac{1}{2} \ \mathrm{sgn}\left(m_0 + 2m_1\right) + \frac{1}{2} \ \mathrm{sgn}\left(m_0 - 2m_1\right), \tag{36}$$

$$C_{VM3} = \sum_{n_x=\pm 1, n_y=\pm 1} n_x n_y C_M\left(n_x, n_y\right) = \frac{1}{2} \ \mathrm{sgn}\left(m_0 + 2m_1\right) + \frac{1}{2} \ \mathrm{sgn}\left(m_0 - 2m_1\right) + \mathrm{sgn}\left(m_0\right), \tag{37}$$

where two of them become identical due to the C_4 symmetry, $C_{VM1} = C_{VM2}$. We note that the concept of the valley–mirror-Chern number is lost at higher energy far away from the Fermi level, where the Dirac Hamiltonians merge into the tight-binding Hamiltonian.

The thin film is a topological insulator indexed by the mirror-Chern number and the valley–mirror-Chern numbers in the absence of the electric field ($E_z = 0$). They are symmetry-protected topological numbers since they are no longer quantized when the mirror symmetry is broken by switching on the electric field ($E_z \neq 0$) as in (31).

3.2. Nanoribbons

With the tight-binding Hamiltonian to hand, we are able to demonstrate the band structure of nanoribbons, as shown in figure 3 for various values for parameters m_0 and m_1. We have set $E_z = 0$. We take the direction of the nanoribbon as the x-axis. The momentum component k_x in the bulk band gives the momentum k of the nanoribbon, while the momentum component k_y is quantized. Accordingly, the X and M points are projected to the same momentum $k = \pi$, while the Y and Γ points are projected to $k = 0$. The projected view of the bulk band shown in figure 3(b) is the same as the band structure of the nanoribbon except for the edge states. Namely we can identify the edge states by comparing the projected band structure of the bulk band and the band structure of the nanoribbon. The edge states are shown in magenta in figures 3(c) and (d).

We examine the bulk–edge correspondence. We have shown that the system is indexed by the mirror-Chern number and the valley–mirror-Chern numbers. However, since the valley degree of freedom is ill defined in the vacuum, there is no bulk–edge correspondence for them [31]. Indeed, gapless edge modes emerge when a nanoribbon has a nonzero mirror-Chern number C_M. It is interesting that the gapless edge states emerge at $k = 0$ for $C_M > 0$ and at $k = \pi$ for $C_M < 0$. There are no edge states when the system is trivial ($C_M = 0$). There is an exactly one to one correspondence between the mirror-Chern number C_M and the appearance of edge states in the band structure of a nanoribbon.

The nonzero mirror-Chern number indicates 'quantum mirror-Hall effects'. However it is a highly nontrivial task to experimentally detect the 'mirror-Hall conductivity' since 'mirror-Hall currents' convey neither charge nor spin. On the other hand, there emerge $|C_M|$ gapless states in the edges of a nanoribbon made of a topological insulator with the mirror-Chern number C_M. Without the electric field, these edge states transport merely the mirror charge M. Once we apply external electric field parallel to the nanoribbon direction, one edge state contributes one quantum unit to the electric conductance, as we show in figure 4(d1). Hence we are able to determine the absolute value of the mirror-Chern number by measuring the conductance.

3.3. The electric field and conductance

We switch on the electric field E_z between the front and back surfaces in order to control the edge modes and the conductance in nanoribbons (figure 4(a)). The mirror symmetry is broken by the electric field as in (12).

We show the band structure of a nanoribbon under the electric field E_z in figures 4(b) and (c). The edge states become gapped due to the mixing of the right- and left-going edge states as a result of the mirror-symmetry breaking.

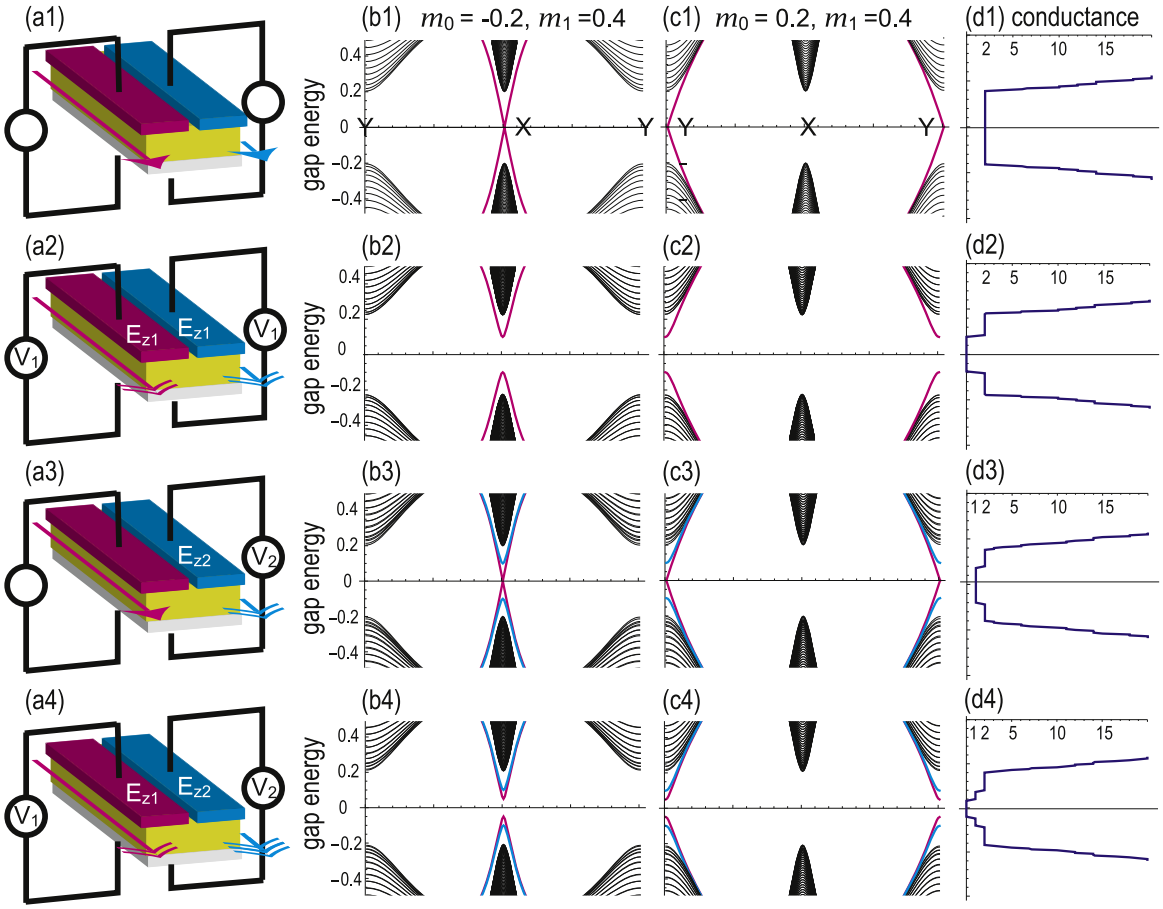

Figure 4. Multi-digit topological transistor, edge modes and conductance for the square lattice. (a) We apply electric fields independently to the right and left edges of a nanoribbon. ((b), (c)) Gapless edge modes emerge without electric fields since they are protected by the mirror symmetry. The gap can be controlled using an electric field independently on the right and left edges. (d) We have calculated the conductance as a function of the gap energy. The conductance can take quantized values 0, 1 and 2 as in (d4), hence providing us with a basic mechanism of a multi-digit topological transistor.

The gapless edge mode transports the electric current. In order to calculate the conductance we separate a nanoribbon into three parts: the left (L) lead, the device (D) and the right (R) lead. The low-bias conductance $\sigma\left(E\right)$ at the Fermi energy E is given by [56]

$$\sigma\left(E\right) = \frac{e^2}{h}\ \mathrm{Tr}\left[\Gamma_{\mathrm{L}}\left(E\right)G_{\mathrm{D}}^{\dagger}\left(E\right)\Gamma_{\mathrm{R}}\left(E\right)G_{\mathrm{D}}\left(E\right)\right], \tag{38}$$

where $\Gamma_{\mathrm{R(L)}}\left(E\right) = \mathrm{i}\left[\Sigma_{\mathrm{R(L)}}\left(E\right) - \Sigma_{\mathrm{R(L)}}^{\dagger}\left(E\right)\right]$ with the self-energies $\Sigma_{\mathrm{L}}\left(E\right)$ and $\Sigma_{\mathrm{R}}\left(E\right)$, and $G_{\mathrm{D}}\left(E\right)$ is the single-particle Green function of the device,

$$G_{\mathrm{D}}\left(E\right) = \frac{1}{E - H_{\mathrm{D}} - \Sigma_{\mathrm{L}}\left(E\right) - \Sigma_{\mathrm{R}}\left(E\right)}, \tag{39}$$

with the Hamiltonian $H_{\rm D}$ of the device region. The self-energy $\Sigma_{\rm L(R)}(E)$ describes the effect of the electrode on the electronic structure of the device, where the real part results in a shift of the device levels while the imaginary part provides a lifetime. It is to be calculated numerically [12, 54, 57–59].

We have calculated the conductance in the presence of E_z, which we show in figure 4(d). The conductance near the Fermi energy is 2 for $E_z = 0$ (figure 4(d1)) since the edge states are doubly degenerate. Once we turn on the electric field, the conductance falls to zero since the edge states disappear due to the anticrossing (figure 4(d2)). Namely, it acts as a field-effect transistor [42]. It is possible to apply different electric fields E_{z1} and E_{z2} to the right and left edge states (figure 4(a)). The conductance can be 0, 1 and 2, which forms a multi-digit field-effect topological transistor (figure 4(d4)). The conductance is quantized and topologically protected.

4. The triangular lattice with C_6 symmetry

We proceed to study the triangular lattice with the C_6 symmetry. Note that the triangular lattice has hexagonal symmetry. By substituting $N = 3$ into the Hamiltonian (4), and taking only the nearest neighbor sites ($\ell = 1$), we obtain

$$A_x = -2\lambda_1\left[\sin\frac{k_x}{2}\cos\frac{\sqrt{3}k_y}{2} + \sin k_x\right], \tag{40}$$

$$A_y = -2\sqrt{3}\lambda_1\cos\frac{k_x}{2}\sin\frac{\sqrt{3}k_y}{2}. \tag{41}$$

We show the band structure in figure 5. There are six massless Dirac cones, in which one Dirac cone resides at the Γ point, three Dirac cones at the M points and two Dirac cones at the K and K′ points. In the vicinity of each Dirac cone, we obtain the low-energy Dirac theory

$$A_x = v_x k_x, \quad A_y = v_y k_y, \tag{42}$$

with a set of velocities (v_x, v_y) as $(-3\lambda_1, -3\lambda_1)$ for Γ, $(-\lambda_1, 3\lambda_1)$ for M_1, $(3\lambda_1/2, 3\lambda_1/2)$ for K and K′. The chiralities of the Dirac cone at the Γ, K and K′ points are identical, while the three M points have opposite chirality. This is in contrast with the case of graphene, where the chiralities of K and K′points are opposite.

We show the band structure of nanoribbons in figure 5. It is interesting that there exists a flat band in the region $-\pi \leqslant k \leqslant -\frac{2\pi}{3}$ and in $\frac{2\pi}{3} \leqslant k \leqslant \pi$: see figure 5(f1). One is connecting the K and M points, and the other is connecting the K′and M points.

Like for the square lattice, we introduce the mass term (9) to the Hamiltonian. The leading and the next-to-leading terms are

$$m = m_0 + 4m_1\sin\frac{k_x}{2}\left[\cos\frac{\sqrt{3}k_y}{2} - \cos\frac{k_y}{2}\right]. \tag{43}$$

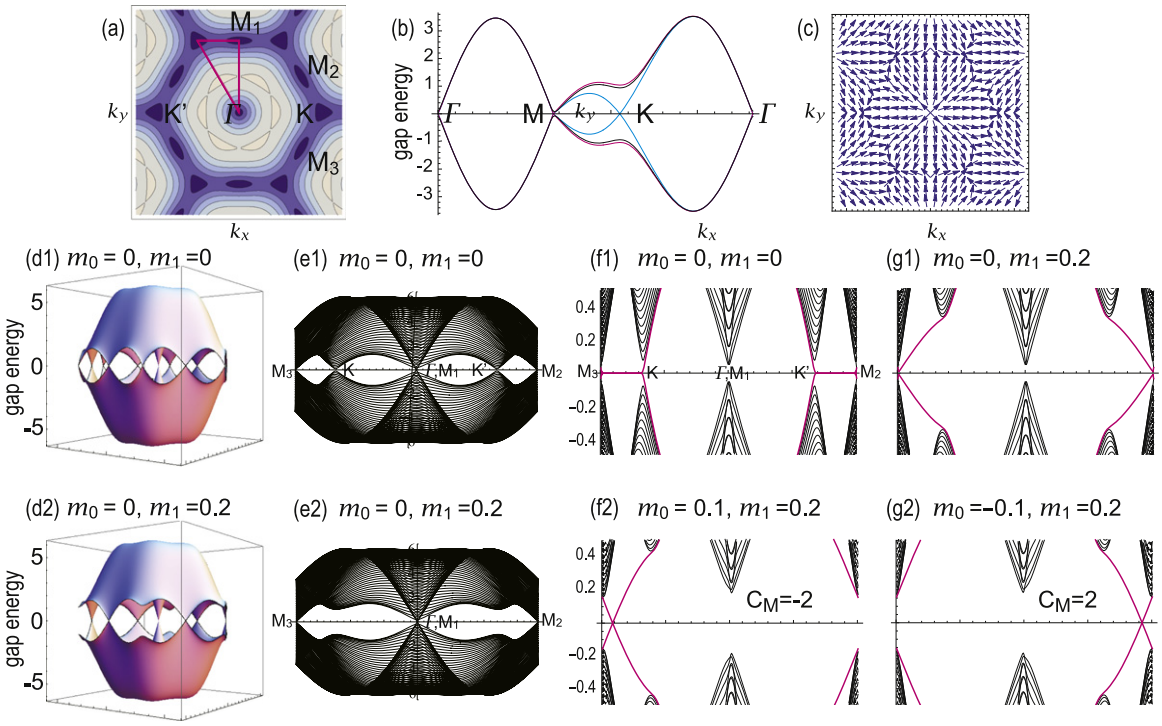

Figure 5. Band structure and spin direction for the triangular lattice. (a) A contour plot of the band structure of the Hamiltonian (8) on the triangular lattice. We have set $\lambda_1 = 0$, $m_1 = m_2 = 0$. The energy is lower in darker regions. (b) The band structure along the lines shown in red in (a). We have set $\lambda_1 = 1$ for all three curves. Cyan curves are for $m_1 = m_2 = 0$. Magenta curves are for $m_1 = 0.2$, $m_0 = 0$. Black curves are for $m_1 = 0.2$, $m_0 = 0.1$. (c) The spin direction in the thin film with the C_6 symmetry for the whole Brillouin zone. (d) Bird's eye views and (e) projected views of the bulk band structure. ((f), (g)) The band structure of nanoribbons, where the gapless edge states are depicted using magenta curves. They emerge in topological insulators with nonzero mirror-Chern numbers. We have taken $\lambda_1 = 1$ in all figures. The values of m_0 and m_1 are indicated in each figure. The vertical axis is the energy in units of λ_1 in all figures. The horizontal axes are $-\pi < k_x \leqslant \pi$, $-\pi < k_y \leqslant \pi$ in (d), $-\pi < k_x \leqslant \pi$ in (e), $-\pi < k \leqslant \pi$ in (f) and (g).

On introducing the mass term, the Dirac cones at the K and K′ points become gapped. The resultant spectrum has four Dirac cones, in which one Dirac cone resides at the Γ point and the other three Dirac cones are at the M points.

Since there are six spin-degenerate Dirac cones, we have the mirror-Chern number and the five valley–mirror-Chern numbers subject to the C_6 symmetry. The mirror-Chern number is given by

$$C_M = \frac{1}{2}\ \mathrm{sgn}\left(m_0 + 3\sqrt{3}m_1\right) + \frac{1}{2}\ \mathrm{sgn}\left(m_0 - 3\sqrt{3}m_1\right) - \mathrm{sgn}\left(m_0\right). \tag{44}$$

This should be compared with the mirror-Chern number (34) for the square lattice with the C_4 symmetry. It follows that the phase diagram is essentially given by the same form as for figure 3(e).

We show the band structure of nanoribbons in figure 5 in the presence of the mass term (43). The flat bands turn into the dispersive edge modes. The position of the edge modes is between the K (K′) and $M_2 = M_3$ points when $C_M < 0$ ($C_M > 0$). As in the case of the square lattice, there is a perfect agreement between the mirror-Chern number and the edge states of nanoribbons, as dictated by the bulk–edge correspondence.

5. Discussion

The minimal tight-binding Hamiltonian of a TCI thin film is a four-band model, in order to take into account the spin and pseudospin (surface) degrees of freedom. We have constructed such a model on the basis of a symmetry analysis. The prominent features are that gapless Dirac cones emerge at all the high-symmetry points and that we can provide them with gaps phenomenologically at our disposal.

We have analyzed the square lattice with the C_4 symmetry and the triangular lattice with the C_6 symmetry in detail. The results may well describe the thin films made of the [001] surface (C_4 symmetry) and the [111] surface (C_6 symmetry) made of $Pb_xSn_{1-x}Te$, by choosing the mass parameters appropriately. According to experimental observations and a first-principles calculation, there are large gaps at the Γ and M points in the [001] surface [37–39, 42]. This is realized by taking a large value of m_1 in our model. On the other hand there are small gaps at the X and Y points, which is taken care of by introducing a small value of m_0.

We may similarly discuss the square lattice with the C_2 symmetry, with the mass term being $m = m_0 + m_1 \cos k_x$. When $m_0 = m_1$, there are Dirac cones only at X and M points, as is consistent with theoretical results [42, 47] on the [110] surface of $Pb_xSn_{1-x}Te$. The model with the C_3 symmetry is also constructed on the honeycomb lattice. We find Dirac cones at the K and K′ points and two degenerate Dirac cones at the Γ point.

Our basic Hamiltonian consists of SOI of the type $\sigma \cdot \boldsymbol{d}_{ij}^{\ell}$ as in (4). We have made this choice since it reproduces the low-energy Dirac theory [42]. The same spectrum is obtained even if we take a SOI of the Rashba type $\sigma \times \boldsymbol{d}_{ij}^{\ell}$ as in (3), although the low-energy Dirac theory now reads

$$H_X = \left(v_1 k_y \sigma_x + v_2 k_x \sigma_y\right)\tau_y + m\tau_x, \tag{45}$$

$$H_Y = \left(v_2 k_y \sigma_x + v_1 k_x \sigma_y\right)\tau_y + m\tau_x, \tag{46}$$

and is different from (22). We predict that another TCI may be found in the future, where the Rashba-type Hamiltonian (3) plays the basic role.

In passing, we make comments on similarities between TCI thin film and silicene. In both cases, we can control the band gap externally by applying an electric field. Furthermore, both have the valley degree of freedom. Nevertheless, there are two main differences. One is that the roles of the perpendicular electric field are very different. For TCI thin film, it acts as a mirror-symmetry breaking term. As a result, the edge state disappears in the presence of the external electric field. In the case of silicene, it does not act as a symmetry breaking term, where there is symmetry whether the spin s_z is a good quantum number or not. As a result, the edge state does not disappear in the presence of the electric field. Second, the electric field induces a topological phase transition in silicene since it may compete with the spin–orbit interaction. On the other

hand, it does not induce a topological phase transition in TCI thin film since the electric field is off-diagonal with respect to the other terms.

A TCI thin film may be used to design a nanodevice for topological electronics. Edge states can be gapped by applying electric fields independently to the right and left edges. We have proposed a multi-digit field-effect topological quantum transistor with the use of gapless edge states of a TCI thin film nanoribbon. This could be a basic component of future topological quantum devices. Our results open up a new route to electric-field-controllable topological electronics.

Acknowledgements

I am very grateful to N Nagaosa, L Fu and T H Hsieh for many helpful discussions on the subject. This work was supported in part by a Grant-in-Aid for Scientific Research from the Ministry of Education, Science, Sports and Culture No. 25400317.

References

[1] Hasan M Z and Kane C 2010 *Rev. Mod. Phys.* **82** 3045
[2] Qi X-L and Zhang S-C 2011 *Rev. Mod. Phys.* **83** 1057
[3] Kane C L and Mele E J 2005 *Phys. Rev. Lett.* **95** 146802
[4] Fu L, Kane C L and Mele E J 2007 *Phys. Rev. Lett.* **98** 106803
[5] Qi X-L, Hughes T L and Zhang S-C 2008 *Phys. Rev.* B **75** 121306
[6] Bernevig B A, Hughes T L and Zhang S-C 2006 *Science* **314** 1757
[7] Rycerz A, Tworzydlo J and Beenakker C W J 2007 *Nat. Phys.* **3** 172
[8] Xiao D, Yao W and Niu Q 2007 *Phys. Rev. Lett.* **99** 236809
[9] Akhmerov A R and Beenakker C W J 2007 *Phys. Rev. Lett.* **98** 157003
[10] Yao W, Xiao D and Niu Q 2008 *Phys. Rev.* B **77** 235406
[11] Xiao D, Liu G-B, Feng W, Xu X and Yao W 2012 *Phys. Rev. Lett.* **108** 196802
[12] Li X, Cao T, Niu Q, Shi J and Feng J 2013 *Proc. Natl Acad. Sci.* **110** 3738
[13] Ezawa M 2012 *Phys. Rev.* B **86** 161407(R)
[14] Ezawa M 2013 *Phys. Rev.* B **87** 155415
[15] Mak K F, Lee C, Hone J, Shan J and Heinz T F 2010 *Phys. Rev. Lett.* **105** 136805
[16] Splendiani A, Sun L, Zhang Y, Li T, Kim J, Chim C-Y, Galli G and Wang F 2010 *Nano. Lett.* **10** 1271
[17] Zeng H, Dai J, Yao W, Xiao D and Cui X 2012 *Nat. Nanotech.* **7** 490
[18] Cao T *et al* 2012 *Nat. Commun.* **3** 887
[19] Mak K F, He K, Shan J and Heinz T F 2012 *Nat. Nanotech.* **7** 494
[20] Wu S *et al* 2013 *Nat. Phys.* **9** 149
[21] Gu Z-C and Wen X-G 2009 *Phys. Rev.* B **80** 155131
[22] Gu Z-C and Wen X-G 2012 arXiv:1201.2648
[23] Turner A M, Pollmann F and Berg E 2011 *Phys. Rev.* B **83** 075102
[24] Chen X, Liu Z-X and Wen X-G 2011 *Phys. Rev.* B **84** 235141
[25] Pollmann F, Berg E, Turner A M and Oshikawa M 2012 *Phys. Rev.* B **85** 075125
[26] Ezawa M 2014 *Phys. Lett.* A **378** 1180
[27] Ezawa M 2012 *New J. Phys.* **14** 033003
[28] Drummond N D, Zolyomi V and Fal'ko V I 2012 *Phys. Rev.* B **85** 075423
[29] Ezawa M 2012 *Phys. Rev. Lett* **109** 055502

[30] Ezawa M 2013 *Phys. Rev. Lett.* **110** 026603
[31] Ezawa M 2013 *Phys. Rev.* B **88** 161406(R)
[32] Padova P, Quaresima C, Avila J, Frantzeskakis E, Asensio M C, Resta A, Ealet B N D and le Lay G 2012 *Phys. Rev. Lett.* **108** 155501
[33] Lin C L, Arafune R, Kawahara K, Tsukahara N, Minamitani E, Kim Y, Takagi N and Kawai M 2012 *Appl. Phys. Express* **5** 045802
[34] Guo Z X, Furuya S, Iwata J I and Oshiyama A J 2013 *J. Phys. Soc. Jpn.* **82** 063714
Guo Z 2013 *Phys. Rev.* B **87** 235435
[35] Fu L 2011 *Phys. Rev. Lett.* **106** 106802
[36] Hsieh T H *et al* 2012 *Nat. Commun.* **3** 982
[37] Tanaka Y *et al* 2012 *Nat. Phys.* **8** 800
[38] Xu S Y *et al* 2012 *Nat. Commun.* **3** 1192
[39] Dziawa P *et al* 2012 *Nat. Mater.* **11** 1023
[40] Tanaka Y, Shoman T, Nakayama K, Souma S, Sato T, Takahashi T, Novak M, Segawa K and Ando Y 2013 *Phys. Rev.* B **88** 235126
[41] Polley C M *et al* 2014 *Phys. Rev.* B **89** 075317
[42] Liu J *et al* 2014 *Nat. Mater.* **13** 178
[43] Fang C, Gilbert M J and Bernevig B A 2014 *Phys. Rev. Lett.* **112** 046801
[44] Liu J, Duan W and Fu L 2013 *Phys. Rev.* B **88** 241303(R)
[45] Fang C *et al* 2013 *Phys. Rev.* B **88** 125141
[46] Okada Y *et al* 2013 *Science* **341** 1496
[47] Safaei S, Kacman P and Buczko R 2013 *Phys. Rev.* B **88** 045305
[48] Wojek B M *et al* 2013 *Phys. Rev.* B **87** 115106
[49] Wang Y J *et al* 2013 *Phys. Rev.* B **87** 235317
[50] Ezawa M 2014 *Phys. Rev.* B **89** 195413
[51] Teo J C Y, Fu L and Kane C L 2008 *Phys. Rev.* B **78** 045426
[52] Takahashi R and Murakami S 2011 *Phys. Rev. Lett.* **107** 166805
[53] Nielsen H B and Ninomiya M 1981 *Phys. Lett.* B **105** 219
[54] Ezawa M 2013 *Appl. Phys. Lett.* **102** 172103
[55] Slager R-J, Mesaros A, Juričić V and Zaanen J 2013 *Nat. Phys.* **9** 98
[56] Datta S 1995 *Electronic Transport in Mesoscopic Systems* (Cambridge: Cambridge University Press)
Datta S 2005 *Quantum Transport: Atom to Transistor* (Cambridge: Cambridge University Press)
[57] Sancho M P L, Sancho J M L and Rubio J 1985 *J. Phys. F: Met. Phys.* **15** 851
[58] Muñoz-Rojas F, Jacob D, Fernández-Rossier J and Palacios J J 2006 *Phys. Rev.* B **74** 195417
[59] Zârbo L P and Nikolić B K 2007 *EPL* **80** 47001
Areshkin D A and Nikolić B K 2009 *Phys. Rev.* B **79** 205430